JOURNAL OF OPTOELECTRONICS AND ADVANCED MATERIALS Vol. 12, No. 8, August 2010, p. 1621 - 1635

Xerographic spectroscopy of gap states: Se-rich amorphous semiconductors

V. I. MIKLA
Institute for Solid State Physics & Chemistry, Uzhgorod National University, Voloshina St.54, 88000 Uzhgorod, Ukraine

Xerographic techniques, initially developed to characterize photoreceptors, are widely applicable to the study of amorphous and photoconductive insulators in a relatively thin and thick film forms. Initially, the high electric field (10^5-10^6 V cm^{-1}) due to corona charging is applied to sample films, and then the decay of the open-circuit surface potential is measured. The xerographic probe technique is a unique means to characterize electronic gap states. In particular, a map of states near mid-gap is determined by time-resolved analysis of the xerographic surface potential.

(Received July 15, 2010; accepted August 12, 2010)

Keywords: Amorphous semiconductors, Selenium, Xerography

1. Introduction

The time-of-flight methods are particularly important but they can not give sufficient information about the whole spectrum of states in the mobility gap of amorphous chalcogenides. Therefore, in addition to conventional time-of-flight (TOF), delayed field time-of-flight (DFTOF), xerographic time-of-flight (XTOF), interrupted field time-of-flight (IFTOF) [1-5], thermally stimulated conductivity (TSC) and thermally stimulated depolarization currents (TSDC) [6-16], other complimentary techniques which probe the gap states are needed. Xerographic techniques which were initially developed to characterize properties of electrophotographic (xerographic) photoreceptors [17], seemed to be direct, suitable, informative, powerful, and widely applicable for the study of amorphous thin films and photoconductive insulator thin films [18].

To investigate charge transport in photoreceptor materials, conventional time-of-flight and its various modifications mentioned above have been used. Below we have focused our attention on xerographic discharge technique. As the initial stage of this experimental technique it is necessary to charge the surface of the examined material to a relatively high voltage. For this purpose corona discharge is used. Therefore, before considering the principle of xerographic spectroscopy technique, we describe the construction and performance of different types of corona devices.

1.1. Corona devices

When a high voltage of several kilovolts is applied to a corona emitter, the field near the emitter exceeds the threshold field for air breakdown. Under this condition the molecules near the emitter become ionized. The ions may carry positive or negative charge. This depends on whether the emitter is at a positive or negative voltage. If insolating material which is supported by earthed metal is placed close to the corona emitter, some of the generated ions migrate to the floating surface of the sample and increase or decrease the surface charge density.

To improve the charging performance, the grounded electrodes are placed around the corona emitter. The structure is called the corona housing and helps direct the ion current and holds the corona emitter. Screen greed is inserted between the corona emitter and the sample to provide better control of charging. This is the corona greed. Several variables are known which determine the efficiency of sample charging. Among these the most important are:

(a) the uniformity of the charge deposited on the sample surface;

(b) the amount of corona current which reaches the sample surface.

Reasonably, the assessment of electrostatic characteristics of the sample examined depends on its particular applications. As for electrophotography, the following may be listed: measuring the charge acceptance (or the maximum surface charging potential), dark decay of the surface potential of the sample charged in darkness, light decay or photoinduced discharge (PID), and so-called residual potential (in other words, the potential which remains on the sample surface after photo-discharge.

There are two, more or less exploited, types of corona devices – a pin corona discharge corona device and a wire corona discharge device. These devices are well-described by Vaezi-Nejad [19].

A pin corona discharge corona device shown in Figure 1consists of a stainless steel rod with a sharp conical tip as the corona emitter, a brass hollow cylinder

as the corona case and a Perspex cup as the corona emitter holder.

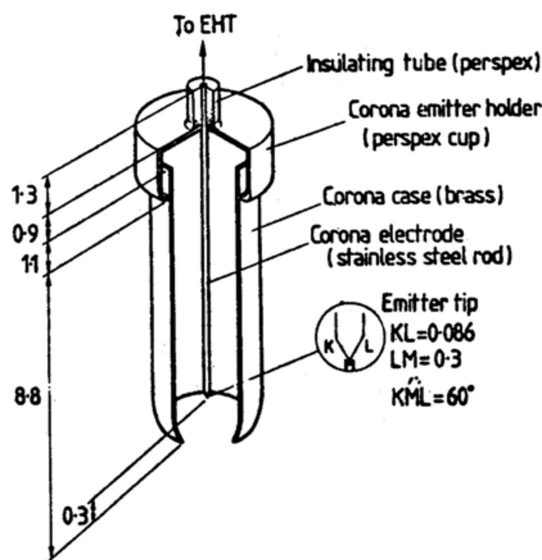

Fig. 1. Schematic presentation of pin corona (dimensions in centimeters) [19]

Corona devices of this type have been used in the past (see e.g. [17]). Latter becomes clear that the electrostatic charging performance of pin corona is unsatisfactory.

To measure the corona current distribution, the experimental apparatus of the type shown in Fig. 2 was devised.

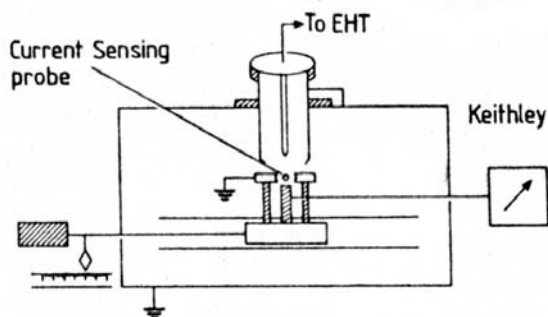

Fig. 2. An apparatus for current distribution measurements

The most important component of this apparatus is the current sensing probe. This is a small aluminum disc (area = 1.77 mm^2) placed in the centre of a relatively large plate (area = 4.2 × 2.6 cm^2). The detecting disc is electrically insulated from the plate by a 0.75 mm air gap. As a disadvantage of a pin corona device it should be mentioned that the current distribution is not uniform.

An alternative to pin corona is a single wire corona (Fig. 3).

A wire corona basically consists of a hollow stainless steel cylinder (inner diameter = 3-5 cm, length = 10.7 cm and thickness = 0.16 cm) as the corona case with a 5.7 cm × 3.0 cm window. Two Perspex slabs of dimensions 5.5 × 3.4 × 1.25 cm were used to hold the corona wire.

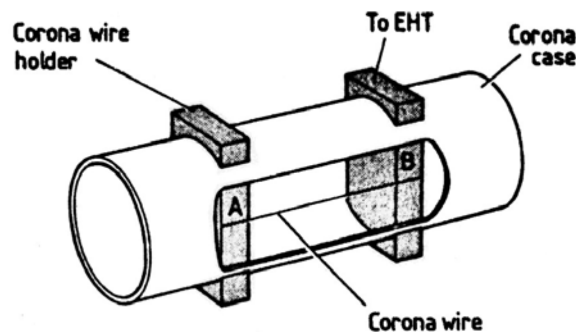

Fig. 3. Schematic presentation of single wire corona. Characteristics and parameters: cylindrical case diameter = 3.5 cm; length of wire = 3.7 cm; wire diameter = 76 μm; wire to window spacing = 1.0 cm; wire to back of the case distance 2.5 cm

The primary requirement for a corona wire emitter is that it should produce ions by means of a corona discharge at a reasonable voltage which is typically 3 -7 kV. In order to achieve high electric field, the wire diameter must be small (less than 100 μm). As the material for corona emitter, tungsten is particularly suitable because of its resistance to the harsh environment created by the corona discharge such as ultraviolet light and various nitrogen-oxygen compounds produced in the discharge. Another advantage of this material is that it is mechanically strong to resist breakage caused by the stress of stringing, handling and cleaning. The corona onset voltage of 1 kV was easily achievable. It is possible to improve a single corona (this type of corona device we have considered above) charging characteristics by adding an identical tungsten wire to the device thus forming a double wire corona discharge. The wires were 3.7 cm long and spaced by 0.5 cm one another [19].

In an attempt to find most efficient corona discharge device for xerographic spectroscopic purposes, it seems necessary, as Vaezi-Nejad did [20], examine various device configurations utilizing sharp pin/pins and wire/wires as the corona emitter. The schematic sketches of different corona devices are shown in Figure 4.

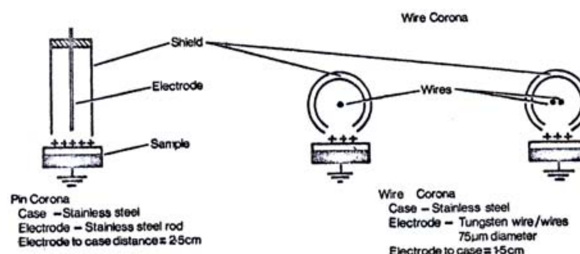

Fig. 4. Corona devices with different configurations [20]

Experimental results obtained [20] illustrate clearly that devices based on thin wires provide a more uniform charge distribution and thus may be recommended for xerographic time-of-flight spectroscopy. In order to control the sample initial voltage, a biased grid is inserted between the corona emitter and the floating surface of the sample.

After charging the sample, it is necessary to measure exactly the surface potential at various stages. These are the following.

1. **The initial voltage** of the sample for calculation of drift mobility.
2. **The sample voltage after photoexcitation**. One can estimate the total charge injected into the sample. This can be made subtracting the sample voltage (after photoexcitation) from the initial voltage.
3. **The final value of the sample voltage** which is measured after photoexcitation. This is known in the literature as **the residual voltage** and it is due to deeply trapped photoinjected carriers when they transit across the sample. If the sample is repeatedly charged-discharged, the residual voltage builds up with the number of cycles and saturates. In this case we deal with **the saturated residual voltage** and can extract information about the deep traps.

After charging, the decay of the open-circuit surface potential is measured. From these measurements important information can be extracted. In last decades the xerographic probe technique becomes a very popular and unique means to characterize electronic gap states. In particular, a map of states near mid-gap is determined by time-resolved analysis of the xerographic surface potential [21,22].

1.2. Principle of Xerographic measurements technique

An optimal photoreceptor design will require, among many other factors, high charge acceptance, slow dark discharge, low first and cycle-up (saturated) residual voltages, and long carrier ranges ($\mu\tau$). The later factor has been addressed above.

In general, the dynamic behavior of electrophotographic potentials developed at two important stages in the xerographic cycle: immediately after charging in the dark (dark decay), and then immediately after photodischarge (i.e., residual decay). Both are extraordinarily sensitive to bulk space-charge fluctuations. In fact, 10^{12} cm^{-3} uniformly trapped electrons can, in a typical sample film, give rise to several volts of surface potential which is easily measured. From xerographic measurements, especially from time-resolved analyses, information can be extracted about electronic gap states which determined the photoelectronic behavior of amorphous chalcogenides.

There are essentially three important types of xerographic behavior. They are generally termed:

(a) **the dark discharge;**
(b) **first cycle residual**
(c) **the cycle-up residual voltage**.

All must be considered in evaluating the electrophotographic properties, e.g. of a-Se and its alloys. It should be stressed that these three parameters is extremely informative in the sense to map band-gap states.

In the sensitization-exposure part of the xerographic cycle, as illustrated in Fig. 1.4, a photoreceptor film mounted on a grounded substrate is charged to a voltage V_0 by corona then completely photodischarged by exposure to strongly absorbed light (absorption depth $\delta \ll L$). Both the top corona contact and the substrate contact should be blocking. The resulting capacitor-like structure contains a uniform field after charging in the dark. Illumination with strongly absorbed light creates a thin sheet of electron-hole pairs which separate under action of field. Depending on charging polarity one sign of carrier acts to neutralize charge on the top surface while the opposite sign of carrier drift through the bulk toward the grounded surface. As a result of this carrier displacement the surface voltage decays in time: this is called photoinduced discharge. Ideally, the surface voltage would decay to zero. What really happened is that some fraction of carriers becomes deeply trapped during transit through the bulk. Reasonably, at the end of the illumination, there is a measurable surface potential termed the residual potential V_R. Space-charge neutrality is finally reestablished by thermally stimulated process but on a longer time scale.

It should be noted that there is important information yielded at each stage of the xerographic cycle. This information consists in the following.

1. By time resolving the charge delivered to an amorphous film from a corona, one can discern injection phenomena and measure dielectric parameters.
2. By measuring the temperature-dependent dark decay of surface voltage, one can determine the energy distribution of thermal generation centers. This later technique or the measurements of the dark discharge depletion time, which is the time, required for the bulk to generate some fixed quantity of charge under isothermal condition, one can estimate the position of the Fermi energy. The details of depletion discharge we consider latter.
3. Analysis of photoinduced discharge can be used to determine the parameters which characterize photogeneration and transport processes.
4. From analysis of residual buildup during repetitive cycling and from analysis of isothermal decay of xerographic residual after cycling ceases, it is possible to map the spectral distribution of bulk traps in an amorphous film.

Corona-mode xerographic measurements were carried out using a reciprocating sample stage. In operation the sample is first passed under a corona-charging device, the corotron, which can be set to deposit either positive or negative ions on the sample surface. The charging circuitry is such that constant current can be supplied to the sample, simplifying the residual voltage cycle-up and in some cases xerographic time-of-flight data. After charging, the sample is moved to a measuring

station and the surface voltage is determined using a transparent, capacitively coupled electrometer probe. The time interval between termination of the charging and the onset of surface voltage measurement is a few tenths of seconds. Either the dark decay or the photoinduced-discharge characteristic (PIDC) following step or flash illumination with strongly absorbed light, can be measured. After discharge, decay of residual potential can be time- resolved. The entire sequence of charging, photodischarge, and residual can be continuously recycled. As a consequence, one can observe the progressive, stepwise buildup of residual voltage. The contacts are blocking in the sense that they allow the samples to charge capacitively in the dark for both positive and negative corona.

Dark discharge rate must be sufficiently low to maintain ample amount of charge on the photoreceptor during the exposure and development steps. A high dark decay rate will limit the available contrast potential. The residual potential remaining after the xerographic cycle must be small enough not to impair the quality of the electrostatic image in the next cycle. Over many cycles, the cycle-up residual potential should be small, to avoid deterioration in the copy quality after many cycles.

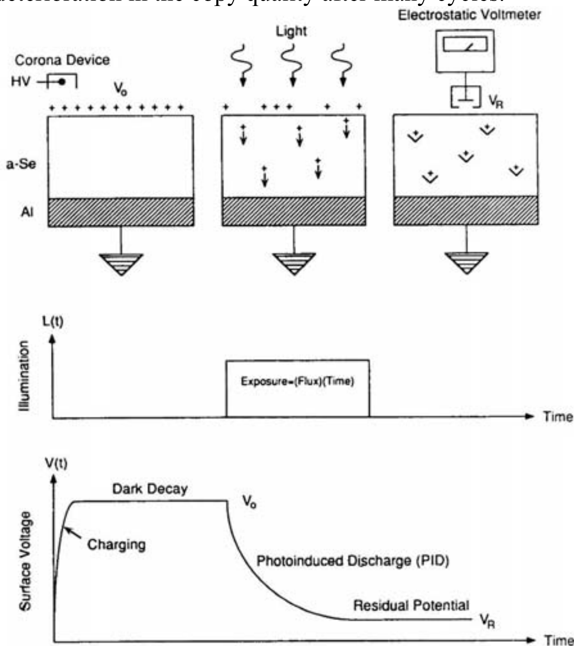

Fig. 5. The xerographic measurements technique (schematic illustration) [18].

In the case of a-Se, these xerographic properties have been extensively studied by numerous authors. In addition to the magnitude of the saturated residual voltage, the rate of decay and the temperature dependence of the cycle-up residual potential are important considerations, since they determine the time required for the photoreceptor to retain its first cycle xerographic properties.

Fig. 6 displays the simplest experimental setup for xerographic measurements. The rotating photoreceptor drum is charged at station A by a corotron device. The surface potential is measured at B, and the photoreceptor is then exposed to a controlled wavelength and intensity illumination at station C, following which its surface potential is measured again at a station D. In some systems, the surface potential is also monitored during exposure at C via a transparent electrometer probe to study the photoinduced discharge characteristics. Normally, the charging voltage, speed of rotation, and exposure parameters such as energy and wavelength are user-adjustable.

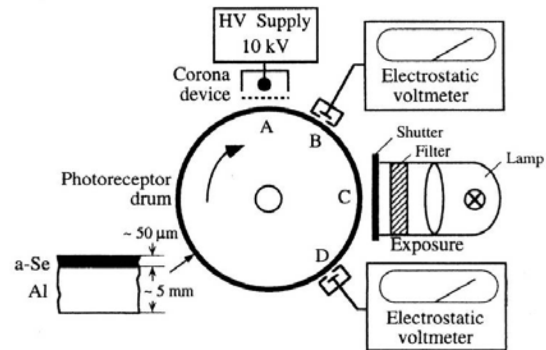

Fig. 6. Simplified schematic diagram of a xerographic measurement. The photoreceptor is charged at A and exposed at C. Its surface potential is measured before and after exposure at B and D [18].

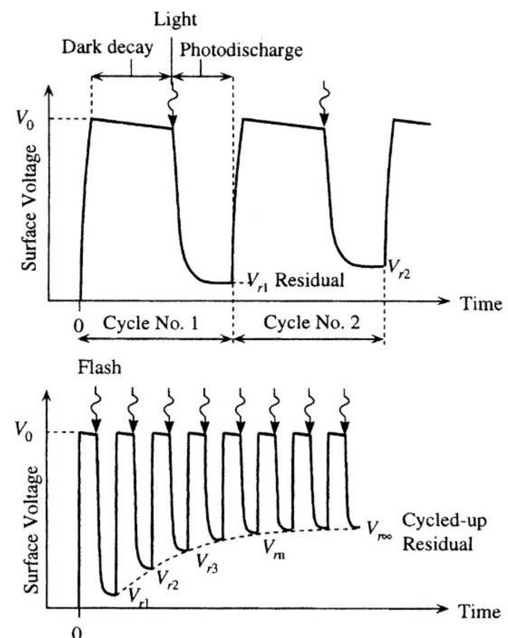

Fig. 7. Typical photoreceptor behavior through xerographic cycles showing dark decay, first cycle residual potential V_{r1}, and cycle-up residual potential V_{rn} after many cycles [18].

The residual potential can be related to the space-charge density. For the case of uniform bulk space-charge of density ρ_0, we may write [21] the simplified expression for residual potential V_r

$$V_r = \rho_0 L^2/2\varepsilon_0\varepsilon = Ne\ L^2/2\varepsilon_0\varepsilon, \qquad (1)$$

where L is the sample thickness, ε is the relative dielectric constant, ε_0 the free-space permittivity, N is the number per unit volume of electronic charges e. A relatively small density of surface or bulk-trapped charges on or in typical xerographic film can give rise to an appreciable surface voltage (Fig. 8) [21].

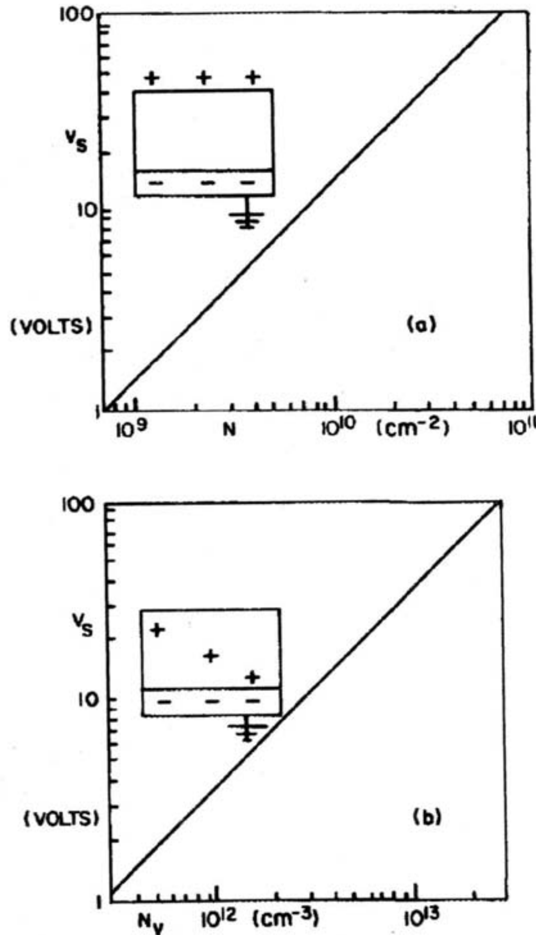

Fig. 8. (a) Surface voltage V_s vs surface density of electronic charges (top). (b) Surface voltage V_s vs volume density of electronic charges (bottom). Both computed using Eq. 1 for a 50 μm thick film, ε = 6.4 [21]

The μτ product where μ is the drift mobility and τ the bulk deep trapping lifetime can be determined from first-cycle residual potential of a well-rested sample of thickness L. In the weak trapping limit (when the residual V_r is much less than the charging voltage V_0) Kanazawa and Batra [23] derive the expression

$$V_r/V_0 = (0.5\ L^2/\mu\tau\ V_0)[-\ln(2\ V_r/V_0). \qquad (2)$$

The physically plausible expression derived by taking the residual to be that voltage for which the carrier range is nominally half the sample thickness

$$V_r/V_0 \approx 0.5\ L^2/\mu\tau\ V_0. \qquad (3)$$

In the strong trapping limit ($V_r \sim V_0$) Kanazawa and Batra [23] derive

$$V_r/V_0 = 1 - (\mu\tau\ V_0/L^2)(\ln 2), \qquad (4)$$

which differs only slightly from the expression based on the above physical definition of residual

$$V_r/V_0 = 1 - (\mu\tau\ V_0/L^2). \qquad (5)$$

It should be noted here that bulk deep trapping lifetimes computed from first-cycle residuals are in agreement with lifetimes measured in the time-of-flight mode under range-limited conditions. For example [21], in a-Se specimen with L = 48 μm charged to 200 V, hole and electron residuals at T = 295 K were found to be 1.8 and 44 V, respectively. The measured drift mobility, lifetimes, and μτ products, for electrons and holes, respectively, are 4.9×10^{-3} cm^2/V s, 5×10^{-5} s, 2.45×10^{-7} cm^2/V, and 0.16 cm^2/V s, 4.4×10^{-5} s, 7.04×10^{-6} cm^2/V. The μτ product computed using Eq. (4) is 2.62×10^{-7} cm^2/V for electrons and 6.4×10^{-6} cm^2/V for holes [21].

1.3. Dark discharge in a-Se

The surface potential of charged photoreceptor will decay even in the dark. Figure 9 shows typical positive and negative dark discharge curves for pure a-Se films prepared under different conditions. As it can be seen, the dark discharge rate depends on substrate temperature [17].

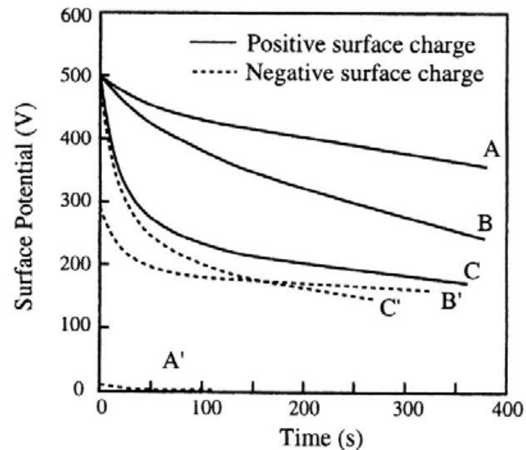

Fig. 9. Dark decay of surface potential on a-Se layers. A, B, and C involves a-Se deposited under different substrate temperature (T_s) conditions: A and A' at T_s = 75 ^{0}C; B and B' at T_s = 50 – 60 ^{0}C; C and C' T_s = 25-50 ^{0}C and uncontrolled [18].

In principle, thermal generation of carriers in the bulk, hole, and electron transport and interfacial injection – all these factors can be the cause of dark decay. The simplest picture of dark decay is one in which electron-hole pairs are thermally generated in the bulk at a rate G_B and swept put rapidly compared with the generation rate [24]. The time-dependent field E can be obtained by setting the sum of the displacement and conduction currents equal to zero:

$$\frac{dE}{dt} = e(J_s + G_B L)/\varepsilon\,, \qquad (6)$$

where J_s is a surface charge generation rate ($cm^{-2}\ s^{-1}$), ε is the bulk dielectric constant and L is the film thickness. As it indicates the form of Eq. (7), a series of measurements on samples of varying thickness are required to distinguish bulk from surface contribution to dark decay [25].

The dark decay in pure and alloyed a-Se films may be caused by all of the above mentioned factors: substrate injection, bulk thermal generation, and depletion. It has been found that that the depletion discharge mechanism dominates. At present, this mechanism is generally accepted [26-32].

Experimental studies of dark discharge performed on various Se-based alloys clearly illustrate that instead of the type of behavior predicted by Eq. (6), dark decay is characterized by two distinct zones of time dependence separated by an abrupt transition (Fig. 10).

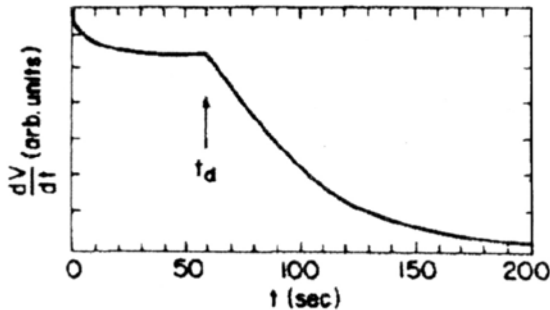

Fig. 10. Typical dark decay (dV/dt vs t) for a-Se film doped with 750 ppmw Cl measured immediately after charging in the dark to 75 V. Thickness 15 μm

This feature can be completely accounted for by a model which presumes that only one sign of carrier is mobile. During dark decay the mobile carrier is depleted (in other words swept out), leaving behind a space charge of opposite sign. Therefore, the dark decay is called a depletion discharge.

In the following, we consider the depletion-discharge model which describes a dark discharge with only one sign of thermally generated charge carrier is mobile on the time scale of experiment. As thermal generation and sweep out of the mobile carrier proceeds, the develops deeply trapped space charge ρ(z) of opposite sign. The time-dependent surface voltage is computed at any time by integrating the instantaneous field across the sample thickness, taking into account of all sources. This procedure directly allows one to distinguish the bulk charge generation process from surface charge losses.

The instantaneous surface potential is given by [25]

$$V = \int_0^{z_0} dz E(z) = \frac{1}{\varepsilon}\int_0^{z_0} dz(\sigma - \int_0^{z0} dz'\rho(z))\,, \qquad (7)$$

where σ is the surface charge density initially deposited, minus any loss by injection up to instant of measurement. Note that Z_0 is the depth (measured from the top surface) at which $E(Z_0)$ is zero and is equal to or less than thickness L. At $Z_0<L$, the surface charge density and Z_0 are related by

$$\sigma = \int_0^{z_0} \rho(z)dz \qquad (8)$$

If depletion is a spatially homogeneous process, Eqs (7) and (8) simplify and the instantaneous surface voltage is then given by

$$V = (\sigma Z_0/\varepsilon) - (\rho Z_0^{\ 2}/2\varepsilon)\,, \qquad (9)$$

where Z_0 and ρ are time dependent.

The process seems to proceed under following scenario. Initially, when the bulk charge is less than the surface charge (σ > ρL), then Z_0 equals L and is time independent. Latter, when Z_0 is less than L, Z_0 equals σ/ρ and is therefore time dependent. As a result, with increasing ρ the parameter Z_0 decreases. Between these zones exists a demarcation defined by the condition

$$\rho L = \sigma\,, \qquad (10)$$

which occurs when t = t_d, where t_d is called the depletion time. The explanation of physical process at depletion discharge is, at the first sight, simple. As charge is uniformly depleted from the bulk of the sample, ρ increases in time until the depleted charge equals the surface charge (Eq. 10). Further depletion now begins to reduce the depleted volume by reducing the dimension Z_0 = σ/ρ < L. As Z_0 shifts toward Z = 0, the region between Z = Z_0 and Z = L retains its space-charge neutrality. The dark discharge rate dV/dt and the surface voltage each exhibit different behavior in the two respective time zones separated by t_d. In zone 1, when t < t_d, one obtains (at condition that there is no surface charge loss)

$$V = \frac{\sigma L}{\varepsilon} - \frac{\rho L^2}{2\varepsilon} \qquad (11)$$

and

$$\frac{dV}{dt} = -\frac{L^2}{2\varepsilon}\frac{d\rho}{dt}\,. \qquad (12)$$

In zone 2, when t > t_d, we obtain

$$V = \sigma^2/2\varepsilon\rho \qquad (13)$$

and

$$\frac{dV}{dt} = -\frac{\sigma^2}{2\varepsilon\rho^2}\frac{d\rho}{dt} \ . \tag{14}$$

From Eq. (5.11), it is clear that $V = V_0 = \sigma L/\varepsilon$ (at $t = 0$)
and (at t_d)

$$V = \sigma L/2\varepsilon = V_0/2 \text{ (when } \rho L = \sigma \text{)} . \tag{15}$$

Therefore, the voltage is reduced to half its initial value at the depletion time. Equations (12) and (14) are modified when surface loss by injection is included by the addition of a surface term, given by

$$(\frac{dV}{dt})_s = \frac{L}{\varepsilon}\frac{d\sigma}{dt} \text{ in zone 1} \tag{16}$$

and

$$(\frac{dV}{dt})_s = \frac{\sigma}{\varepsilon\rho}\frac{d\sigma}{dt} \text{ in zone 2.} \tag{17}$$

The boundary between the zones is defined by condition $\rho(t_d)L = \sigma(t_d)$. It follows that

$$V(t_d) = \frac{\sigma(t_d)L}{2\varepsilon} = \frac{\sigma(t_d)}{\sigma(0)}\frac{V(0)}{2}, \tag{18}$$

where $\sigma(0)$ and $V(0)$ are values at $t = 0$. It should be stressed that the extent to which the surface voltage at t_d has decayed beyond $V_0/2$ thus provides a quantitative measure of the surface loss in specimen.

One representation of $\rho(t)$ is based on the assumption that emission is a first-order rate process. The latter applies to a system containing N_0 (cm^{-3}) discrete emission centers displaced by energy E_0 from the transport state. For this system $\rho(t) \sim t$ because

$$\rho(t) = en = eN_0[1 - \exp(-Rt)], \tag{19}$$

where

$$R = \nu \exp(-E_0/kT) \tag{20}$$

and

$$\rho(t) < eN_0, \quad Rt < 1,$$

thus

$$\rho(t) \approx eN_0 Rt . \tag{21}$$

From Eqs. (10), (20) and (21) it follows that for emission from a discrete center,

$$t_d = (2V_d)\varepsilon / eN_0 L^2 \nu \exp(-E_0/kT), \tag{22}$$

where we abbreviate $V_d = V(t_d)$ so that in this case a plot of $\log t_d$ vs $\log(2V_d)$ should be linear. Any curvature when the log of t_d is plotted against $\log V_0$ (V_0 = surface voltage at t = 0) is then a measure of surface loss by injection. Both features are clearly displayed in Fig. 11.

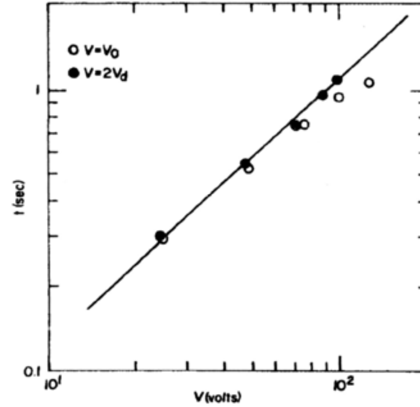

Fig. 11. Dependence of the depletion time t_d on the charging voltage V_0 (open circles) and twice the depletion voltage $2V_d$ (solid circles) for a-Se film doped with 750 ppmw Cl. Thickness 15 μm

Here we note that the scaling of t_d with charging voltage as well as the shapes of the associated depletion curves are observed in a series of Se-rich amorphous alloys and also in pure selenium (in the latter case only in thick, ~ 50 μm, films charged to relatively low voltages at which surface loss was negligible).

In series of elegant experiments Abkowitz et al. [33] demonstrate that the broadening of shallow transport interactive states identified in time-of-flight experiments (see the increasing dispersiveness of time-of-flight transients illustrated by Fig. 12) occur in parallel with a similar process operating on the deep gap states which control the dark decay.

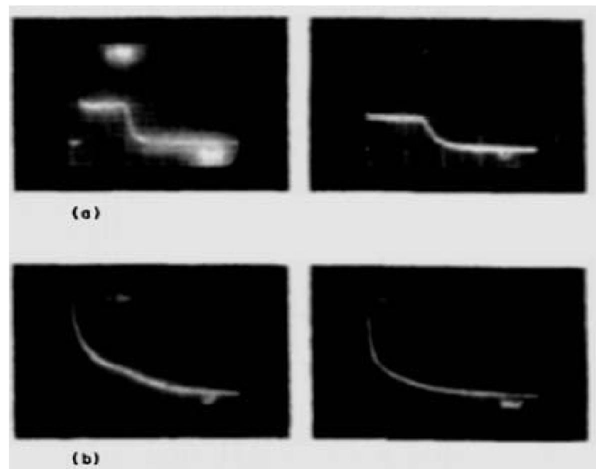

*Fig. 12. Room-temperature transit pulse shapes for holes (left-hand side) and electrons (right-hand side). **(a)** a-Se; E = 10 V/μm; 0.1 μs div^{-1} for holes and 2 μs div^{-1} for electrons. **(b)** 18.4 wt.% Te:Se; E = 17.5 V/μm; 1 μs div^{-1} for holes and 200 μs div^{-1} for electrons.*

The rate at which bulk space charge is uniformly generated may be represented as

$$\rho(t) = at^p, \quad p < 1. \tag{23}$$

This algebraic time dependence is suggested by the analytical modeling of simple cases. Let us consider exponential distribution of emission centers given by

$$N = N_0 \exp(-[E - E_0]/W), \tag{24}$$

which is N_0 at the reference energy E_0, and is also cut off by the Fermi energy for holes (states extending beyond E_F are hole traps rather than emission centers).

It follows that

$$\rho(t) = eN_0(\nu t)^{kT/W}. \tag{25}$$

Here it is assumed that the emission rate prefactor ν does not depend on energy and there is no retrapping. Substituting Eq. (24) into corresponding equations for dV/dt yields

$$\frac{dV}{dt} = -\frac{L^2}{2\varepsilon} a\rho t^{p-1}, \quad t < t_d \tag{26}$$

and

$$\frac{dV}{dt} = \frac{\varepsilon}{2a}(V_0/L)^2 \rho t^{-p-1}, \quad t > t_d. \tag{27}$$

The following distinctive characteristic are now predicted for depletion discharge:

(a) There is an abrupt change in the dark decay rate ($\sim t^{2p}$) at $t = t_d$. The physical origin of t_d - it is the required by the bulk to generate isothermally a quantity of charge equal to the surface charge. This parameter (t_d) provides a quantitative measure of thermal generation.

(b) The sum of the slopes of two linear segments corresponding to $t < t_d$ and $t > t_d$ equals -2.

(c) At $t = t_d$,

$$Lat^p{}_d = \sigma$$

or

$$t_d = (\sigma/aL)^{1/p} = (2V_d\varepsilon/\sigma L^2)^{1/p}. \tag{28}$$

(d) When a series of films differing in thickness L are charged to the same initial field, then a transition from quadratic to thickness-independent behavior will be observed in the dark decay rate at t_d.

Features predicted by Eqs. (26) and (27) are clearly illustrated by Figure 13. A demarcation in the rate of decay is now easily discerned in all cases.

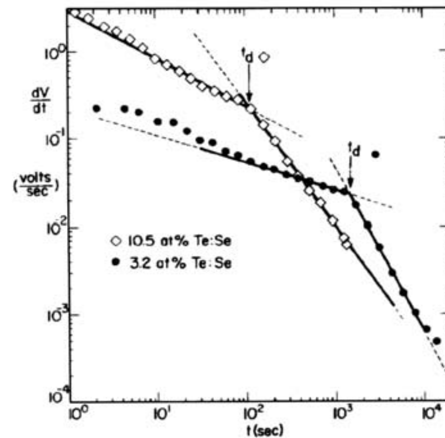

Fig. 13. Dark decay at 297 K of a 3.2 at.% Te:Se film (solid circles) and a 10.5 at.% Te:Se film (diamonds). Films were initially charged to 100 V. Thickness d = 55 μm [25]

In the depletion discharge model, both the shapes of the dark decay and the scaling of the depletion time t_d with the depletion voltage V_d (half the charging voltage in the absence of surface loss) and specimen thickness is completely specified by the p parameter. The form taken by the phenomenological depletion model resembles a key feature predicted in the model proposed by Scher and Montroll [33] for dispersive transport. In the latter model it is the dispersion parameter α which governs a similar scaling law for the transit time. In Figure 14, the depletion time t_d represented on the right ordinate log scale and the p parameter represented linearly on the left are plotted versus composition with samples spanning the range 0-14 at.% in Se.

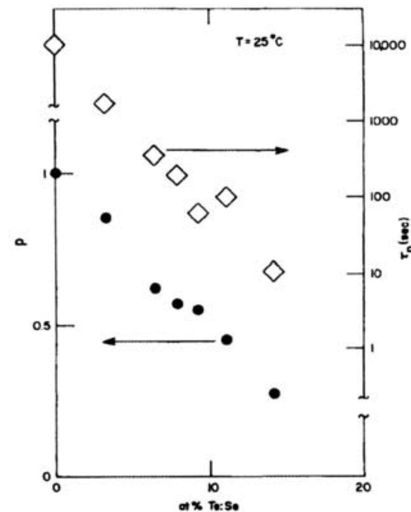

Fig. 14. Composition dependence of the depletion time t_d and the parameter p for Te:Se alloy films [25]

It is clearly seen that under fixed conditions the depletion time decreases exponentially with Te concentration while the p parameter decreases linearly over the same composition range.

The above simple phenomenological model which assumes a power law time-dependent development of spatially uniform negative charge density $\rho(t) = at^p$ can account for all features of the dynamic behavior of the surface potential. Thus when plotted on a log-log scale the $\frac{dV}{dt}$ vs t curve for a wide range of alloy films was found to exhibit a well-defined kink precisely at time t_d when the negative bulk trapped space charge became equal to the surface charge initially deposited. Depletion time t_d provides a measure of the time required by the bulk to generate an experimentally determined quantity of charge. Both the shape of the decay of $\frac{dV}{dt}$ vs t on either side of t_d and the scaling of the depletion time t_d with surface charge σ and sample thickness L, $t_d = (\sigma / aL)^{1/p}$, respectively, provide independent means for measuring parameter p. If the build up in the bulk negative charge density is spatially uniform (as we assume), the internal electric field falls linearly with distance from the top surface. At a certain time t_d, the electric field F at the grounded end of the sample becomes zero. From that time onward the field will be zero at a distance X(t) < L, the sample thickness, and consequently there will be a neutral region from X to L inasmuch as holes generated in 0 < x < X and arriving into X < x < L will not be swept out (Fig. 15). The shrinkage of the depleted volume with time $t < t_d$ means that t_d marks a functional change in the dark decay rate and therefore is readily obtainable from dark discharge experiments.

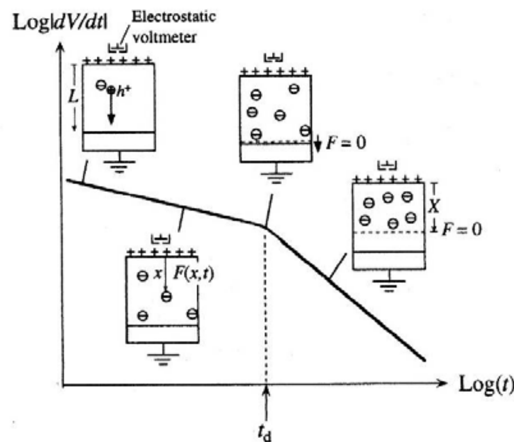

Fig. 15. Typical log-log plot of the dark discharge rate versus time for a wide range of amorphous Se-based alloys

Analysis performed for a range of Se-based alloys reveals that the parameter p and the depletion time t_d scale systematically with alloy composition when experimental conditions remained fixed. Parameter t_d and p decrease with an increase of the concentration of arsenic, antimony or tellurium in the alloy [18,25, 34,35]. The quantity p in the model for dark depletion discharge plays a role analogous to the dispersion parameter α in the theory of dispersive transport [36] of photoinjected carriers.

As it was mentioned above, under low charging voltages the depletion time indicates the time required for the surface potential to decay to half its original value. Under high charging voltages, however, field-enhanced emission from the deep mobility gap centers also plays an important role, and the surface potential initially decays at a much faster rate so that at the depletion time the surface potential is in fact less than half the initial value. Figure 16 shows the dependence of the depletion time t_d and the half-time $t_{1/2}$ on the charging voltage V_0, where it can be seen that at the highest charging voltages there is no improvement in $t_{1/2}$ with further increase in the charging voltage V_0. Inasmuch as the dark decay in Se-based alloys is a bulk process, the rate of discharge increases with the square of thickness $dV / dt \sim L^2$ and can be reduced only by using thin layers. The latter concept leads naturally to the design of multilayer photoreceptor structures.

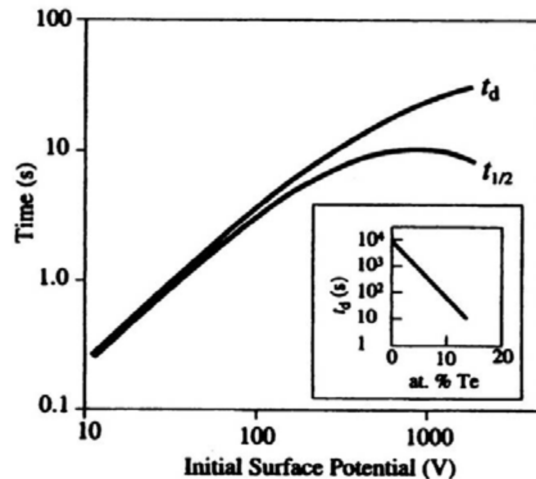

Fig. 16. Log-log plots of the depletion time t_d and time for the surface potential to decay to its half value $t_{1/2}$ versus charging voltage V_0 for an amorphous Se : Te 13 wt% photoreceptor film of thickness 70 μm (from [30]). The inset shows the dependence of the depletion time t_d on the Te content (from [31])

The origin of the deep localized states in the mobility gap that control the dark decay has been attributed to

structural native thermodynamic defects [32,37-39]. Thermal cycling experiments show that the response of the depletion time to temperature steps is retarded, as would be expected when the structure relaxes toward its metastable, liquid-like equilibrium state. As the structure relaxes toward the equilibrium state, t_d decreases further until the structure has equilibrated. The only possible inference is that t_d must be controlled by structure-related thermodynamic defects. The generation of such defects is therefore thermally activated. We should note that since the depletion discharge mechanism involves the thermal emission of carriers from deep localized states, it is strongly temperature dependent. For example, t_d increases in an approximate Arhenian fashion with decreasing temperature. In addition (to the deterioration of the dark decay), there is an increase in the residual potential for a-$Se_{1-x}Te_x$ alloys.

Figure 17 displays the $\mu\tau$ product for holes and electrons [33].

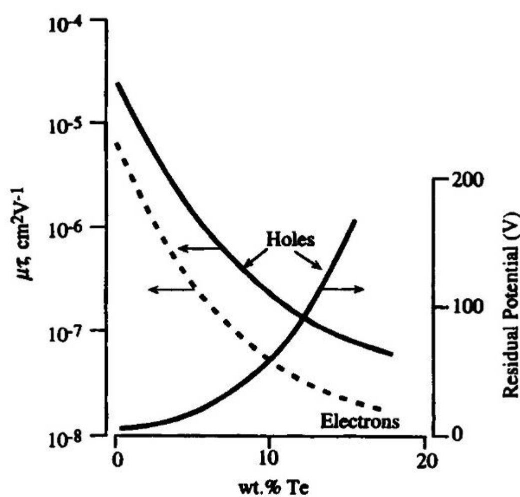

Fig. 17. Hole and electron drift mobility lifetime product $\mu\tau$ and residual potential versus Te content in a-$Se_{1-x}Te_x$ films. The $\mu\tau$ product was xerographically measured by Abkowitz and Markovics [33]; residual potential from [40].

This parameter was determined from xerographic residual potential in a-$Se_{1-x}Te_x$ monolayer films. As one can see, even with very little Te alloying there is a considerable rise in both hole and electron deep traps. The relationship between the trapping time and the residual potential has been evaluated by numerous authors (see, e.g. [23,41]). The residual potential is more than an order of magnitude larger than typical values for pure selenium in the situation when the Te concentration exceeds 12 wt% Te.

Regarding the depletion discharge it should be stressed that with thick films, a good blocking contact between a-Se and the preoxidized aluminum substrate, the depletion mechanism dominates the discharge process. There are several reasons for the experimentally observed fact that amorphous selenium posse good dark decay characteristics. Among these the following may be listed.

1. There are not many deep localized states in the mobility gap of pure amorphous selenium. Saying simply, the concentration of such states are relatively low (less than 10^{12}-10^{13} cm^{-3}).
2. The energy location of these localized states is deep (> 0.8 eV) in the mobility gap. Therefore the thermal generation process of holes and/or electrons from these centers is slow.
3. Injection from the substrate can be reduced substantially by using oxidized Al substrate.

If blue light is used for the discharge process, then the absorption is very close to the charged surface, and one can assume that the discharge process involves the transport of photogenerated holes through the bulk. Trapping of these holes in the bulk then results in the observed first cycle residual potential, V_{r1}. In the case of amorphous selenium photoreceptor films it has been found that V_{r1} is predicted by Warter expression [42]

$$V_{r1} = L^2/(2\mu_d\tau_0)$$

where L is the film thickness, μ_d is the hole drift mobility, τ_0 is the hole lifetime, and $\mu_d\tau_0$ is the hole range.

It can be seen from Fig. 7 that as the xerographic cycle is repeated many times at a constant repetition frequency, the residual voltage rises and eventually saturates. The saturated residual voltage V_{rs} is much larger than the first cycle residual voltage V_{r1}. Both the first residual and the cycle-up saturated residual potential, V_{r1} and V_{rs}, are sensitive to pre-illumination as well as to temperature and alloying. For example, when a-Se films are preilluminated with white light, the buildup of the residual potential occurs more rapidly toward a much higher saturated residual potential. Furthermore, the parameters mentioned (residual potentials V_{r1} and V_{rs}) increase with exposure time. The effects of pre-illumination with band-gap light on the main xerographic characteristics for the case of pure amorphous selenium were examined in details by Abkowitz and Enck in their extensive work [22] and, for Se-rich a-As_xSe_{1-x} alloys, by the present authors [43,44]. Clearly, exposure to white light generates an appreciable concentration of deep hole traps. The effects of pre-illumination we consider in the following paragraph.

There are two possible explanations for the saturation of the residual voltage which seemed to be reasonable [45]. These are given below.

A. The observed saturation may be due to the dynamic balance between trapping and release of charge carriers as the xerographic cycle is repeated.

B. As an alternative variant, it may be due to the filling of the deep trap population so that the saturated residual potential is given by

$$V_{rs} = L^2eN_t/(2\varepsilon_0\varepsilon)$$

where N_t is the concentration of deep traps and ε_0 and ε are, respectively, the absolute permittivity and relative permittivity of the photoreceptor material. The trap-filling interpretation can be verified, by checking whether V_{rs} shows any dependence on the cycling frequency, to exclude a dynamic equilibrium condition involving trap filling and emptying (Fig. 18).

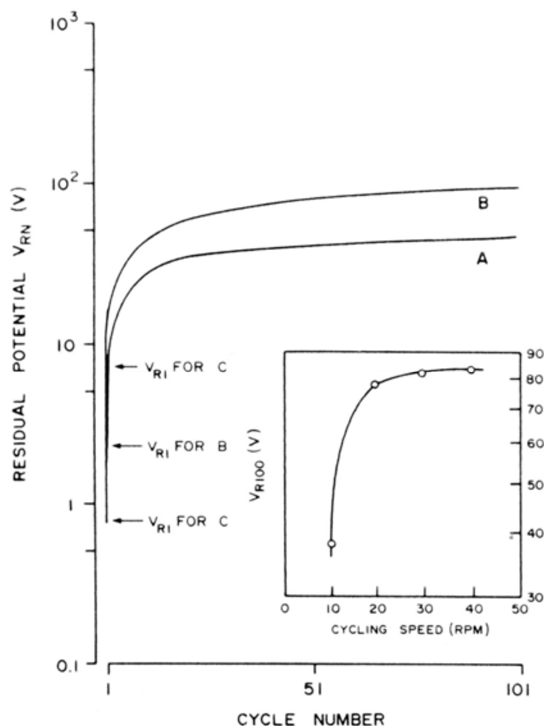

Fig. 18. Typical cycled-up xerographic experiments on a-Se films. The inset shows the dependence of residual potential at the 100th cycle on the cycling speed. Sample A has a lower $\mu\tau$ product than B [46].

The rate of decay and the temperature dependence of the saturated voltage can be used to obtain the concentration and energy distribution of the deep traps responsible for the residual potential. Thus V_{rs} provides a useful means of studying the nature of deep traps in amorphous semiconductors and has been successfully used to derive the energy distribution of deep localized states in the mobility gap of both a-Se and a-Si:H [21,47].

One can assume that the saturated residual potential, at the end of a large number of cycles, decays. As thermal release proceeds, hole are emitted and swept out from the specimen, resulting in the decrease of the measured surface potential. The decay rate of the saturated potential is strongly temperature dependent due to thermal release from deep mobility gap centers, located at approximately 0.9 eV above E_v for holes. The discharge of the saturated potential due to electron trapping occurs much more slowly. The reason is that the energy depth of electron traps from E_c is about 1.2 eV, which is greater than that of hole traps from E_v.

1.4. Photoinduced changes of xerographic characteristics: dark discharge

Amorphous chalcogenide semiconductors exhibit a large spectrum of photoinduced phenomena. According to Keiji Tanaka [48], these unique phenomena observed in chalcogenide glasses can be classified into two main groups.

The first group includes the so-called heat-mode phenomena: the heat generated through nonradiative recombination of photoexcited carriers caused atomic structural changes. The most familiar may be the phase change between crystalline and amorphous phases, which is applied to high-density (more than 1GB) erasable optical memories.

The second is the so-called photon mode. It is well known that for amorphous chalcogenide semiconductors unique effects are characteristic. Reversible thermal and photoinduced changes in amorphous semiconductors have been under active investigation during several decades [48-55]. They are the most unique and intriguing features of chalcogenide vitreous semiconductors. Photoinduced changes appear as nearly parallel shift of the optical absorption edge to lower energy or a reduction in band-gap on exposure to light (so-called "photodarkening"). Such irradiation also causes a change in various physical properties. The physical origin of the processes which takes place at reversible transformations induced by band-gap light and thermal annealing remains unclear. Particular interest is aroused when observations suggest that these changes affect photoelectronic behavior. It is important to note that analysis of changes in photoelectronic properties can be used to relate photoinduced effects to specific changes in the electronic density of gap states.

During the last decades there has been, however, very limited systematic study of photoinduced effects on states, especially of deep lying states in the band gap. In addition, most photodarkening studies have focused upon prototypical binary (and ternary) chalcogenide alloys and relatively little are known about the characteristics of elemental and chalcogen-rich glasses. At the same time, elemental and chalcogen-rich amorphous semiconductors serve as useful model systems for studying the influence of photodarkening on physical properties. Therefore, we consider in the following photoinduced changes of deep levels in pure and selenium-rich amorphous layers.

Careful analysis of the time and temperature dependent decay of the surface voltage on an amorphous film can be used to map the density of states. This procedure can be performed after corona charging of the sample but prior to exposure (known as xerographic dark decay) or after exposure (PID), in the first cycle or after many cycles. The procedure is illustrated for a-As_xSe_{1-x} where residual potential can be measured without complication. Amorphous As_xSe_{1-x} ($0<x<0.20$) is found to be characterized by relatively discrete gap state structure. Measurements performed by the present authors readily discern photo- and thermostructural effects on gap state population (see, e.g. [43,44,52,55] and Refs. therein). Thus, during these structural transformations systematic

variation in the density of localized states distributed throughout the mobility gap are observed. This observation is consistent with the view that native defects play a key role in photoelectronic behavior of amorphous chalcogenides.

The illumination of amorphous As_xSe_{1-x} films by light with energy near the optical gap also causes changes in basic electrophotographic parameters: dark discharge rate, initial charging potential, residual potential, and its dark decay rate. Typical dark discharge curves for film composition $As_{0.2}Se_{0.8}$ are shown in Figure 19.

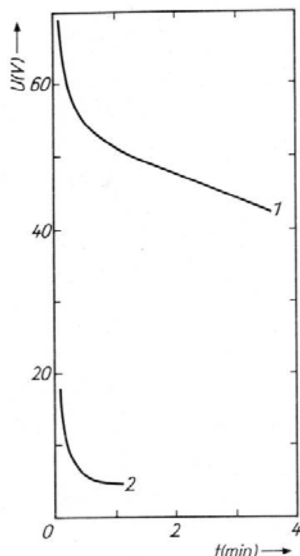

Fig. 19. Dark decay of surface potential in a-$As_{0.2}Se_{0.8}$. (1) Dark-rested sample, (2) after white light exposure 5000 lx × 60 s.

It is apparent that the initial charging voltage U_0 becomes smaller and the surface potential decay rate dU/dt increases after previous photoexcitation. It must be emphasized that, depending on composition, ordinary (changes of either U_0 or dU/dt) or complex (simultaneous changes of U_0 and dU/dt) photoinduced effects may be observable. The former take place in the range 2 to 6 at% As, whereas for the latter concentrations above 8 at% As are needed.

In pure selenium the photoinduced change of discharge rate is comparatively small ($\gamma \approx 1.06$). As the arsenic concentration increases, γ initially becomes progressively larger, then for x > 20 at% As it begins to fall possibly because of the rising dark discharge rate in dark-rested samples. The parameters of dark discharge in dark-rested and photosensitized films are summarized in Table 1. Here $t_{U0}/2$ is the half-decay time, $\Delta U/U_0 = (U_0 - U_0^*)/U_0$ the relative change of the initial charging potential. It is of interest to point out that the "memory" effect (the time interval during which the changes in pre-excited film parameters may be observable) appreciably prolonged with As content: from ≈ 40 min in pure selenium to ≈ 10 h in $As_{0.2}Se_{0.8}$.

Table 1. Surface potential dark decay parameters and their photoinduced changes in As_xSe_{1-x} films.

content	dU/dt (V/s)	$t_{U0/2}$ (s)	γ	$\Delta U/U_0$
0	6.7×10^{-2}	276	1.06	0.30
2	9.7×10^{-2}	150	1.20	-
5	1.4×10^{-1}	138	1.33	-
8	9.3×10^{-1}	19	1.61	-
10	1.22	17	2.3	-
15	1.12	18	3.5	0.50
20	1.4	15	1.9	0.51

* Initial voltage: U_0 = 37 V; thickness: d = 10 μm; T = 293 K; white light exposure: 2000 lx × 120 s.

The ratio $\gamma = (dU^*/dt)/(dU/dt)$ (parameters of irradiated samples are marked by asterisk) is essentially composition dependent.

Fig. 20 shows the time evolution of the dark decay kinetics of the surface potential after photoexcitation. An increasing dark adaptation time, i.e. the dark-resting time of an exposed film before charging it to a certain potential and recording the potential decay, causes a diminishing of the observable photoinduced changes. On the basis of the data in Figure 20, by analogy to the photocurrent transients [43,44], the relaxation functions $\varphi(\tau) = [U_0 - U_0^\tau]/[U_0 - U_0^*]$ and $\zeta(\tau) = [(dU^*/dt) - (dU^\tau/dt)]/[(dU^*/dt) - (dU/dt)]$, characterizing the initial charging potential and the dark decay rate recovery, were estimated (see insert in Fig. 20).

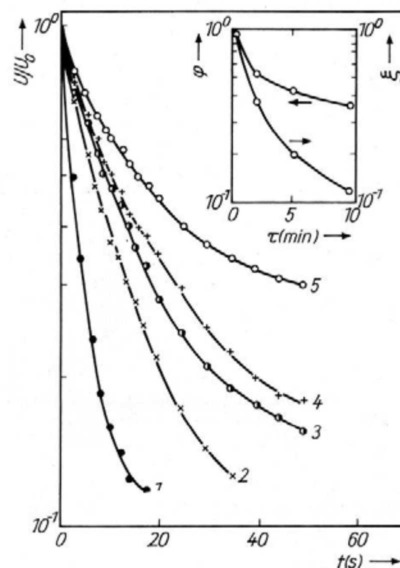

Fig. 20. Dark discharge rate varying with a-$As_{0.15}Se_{0.85}$ sample dark-resting time and corresponding relaxation functions φ(τ), ζ(τ) (insert). (1) τ = 0, (2) 2, (3) 5, (4) 10, (5) 90 min.

It is of particular significance that "memory" effects are influenced not only by variation of composition, but also by electric fields [43, 55-62]. For example, Fig. 21clearly illustrates that the photoinduced change of the dark discharge rate may successfully be "frozen-in" be applying an electric field E ≈ 3 × 10^5 V/cm immediately after light exposure (for comparison, see curves 5 (in Fig. 21a) and 6 (in Fig. 21b).

Dark decay curves of the surface potential in double-logarithmic representation display two distinct rate processes $dU/dt \sim t^{-(1-K)}$ and $dU/dt \sim t^{-(1+K)}$ with cross-over from one regime to the other at $t = t_d$. Detailed analysis of the discharge process shows that t_d shifted to smaller values with increasing As content and after exposure. Note that under low charging voltages U_0 the surface potential at time t_d was approximately half the initial value and that t_d increased with U_0. The features observed in the dark decay study of As_xSe_{1-x} alloy films can be completely accounted for by a depletion discharge model [25-33,43,44]. So, the bulk process driving dark decay is emission and sweep-out of holes from states near mid-gap leading to progressive formation of negative space charge. The rise in dark discharge rate and the shift of t_d with arsenic concentration and photoexcitation may be due to enhanced thermal generation of holes from deep centers. From the temperature dependence of t_d it is estimated that the emitting sites are located at 0.8 to 0.9 eV above the valence band mobility edge.

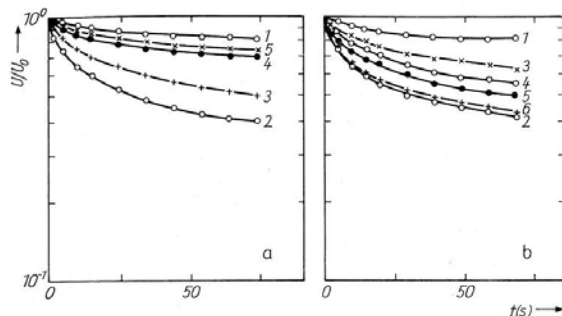

*Fig. 22. Surface potential dark decay in a-$As_{0.1}Se_{0.9}$ films (d = 10 μm). **a)** (1) Dark-rested sample, (2) exposed, (3) to (5) exposed and then dark-rested for 5, 20, and 30 min, respectively. **b)** (1) Dark-rested sample, (2) exposed, (3) to (6) exposed and dark-rested for 30 min in the presence of a surface potential of 115, 170, 215, and 520 V, respectively [43,55].*

1.5. Residual voltage in Se-rich photoreceptors

For the films under examination the residual voltage U_r increases with exposure. For example, previous photoexcitation leads to an increase in U_{r1} (first cycle residual voltage) for Se up to 3.7 V caused by a decrease in $\mu\tau_L$ to 1.3×10^{-7} cm^2 V^{-1}. Taking into account the invariance of μ^e=4.9×10^{-3} cm^2 V^{-1} s^{-1} with light exposure it is obvious that the lifetime reduction (from 5.4×10^{-5} to 2.6×10^{-5} s) is the only reason for photoinduced change.

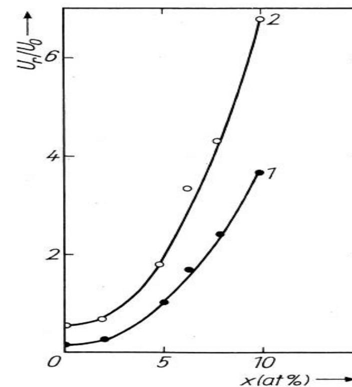

Fig. 23. Dependence of residual voltage after (1) one and (2) five complete xerographic cycles on atomic percentage of As content in amorphous As_xSe_{1-x}

During the continuous repetition of xerographic cycles, the residual voltage U_{rn} at the nth cycle was found to have the typical behavior shown in Fig. 24.

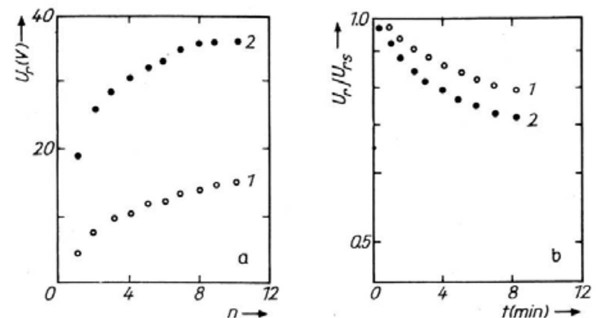

Fig. 24. The build-up in the residual voltage with a) number of xerographic cycles and b) isothermal room-temperature relaxation of saturated residual voltage in (1) dark-rested and (2) photoexcited a-$As_{0.02}Se_{0.98}$ films

The repetition of xerographic cycle leads to the saturation of the residual potential (see Fig. 24). The saturated value, $U_{r\infty}$, corresponds to all the deep traps in the bulk being filled – in pure and Se-rich alloys of amorphous Se this occurs typically after ~ 20-100 xerographic cycles. One can easily check the trap-filling interpretation: if $U_{r\infty}$ shows any dependence on the cycling frequency to exclude a dynamic-equilibrium condition involving trap filling and emptying.

The saturation residual potential U_{rs} (or $U_{r\infty}$) provides [18,25] a measure of the density of uniformly trapped carriers:

$$U_{rs} = Ned^2/2\varepsilon$$

where ε is the dielectric constant. An increase in U_{rs} in pre-exposed films indicates photoenhanced accumulation of charge at deep centers. We obtain N≈10^{15} cm^{-3} and

$N^* \approx 4\times10^{15}$ cm^{-3} for dark-rested and pre-exposed $As_{0.1}Se_{0.9}$ films, respectively [43,44,55].

The residual potential decays to zero. This process is controlled by the spectrum of trap release times. The trap energies can be deduced from an analysis of isothermal residual potential decay curves using

$$U_{rs} = \sum C_i \exp(-t/\tau_i)$$

where $\tau_i^{-1}=\nu_i \exp[-E_i/kT]$ is the release time from the ith trap, ν_i is the frequency factor and E_i is the trap depth. We find that deep levels in amorphous selenium reside at E_i^h = 0.85 eV and E_i^e = 1.0 eV for holes and electrons, respectively. Their depth becomes somewhat shallower with addition of As , e.g. E_i^h = 0.80 eV and E_i^e = 0.90 eV in $As_{0.1}Se_{0.9}$. The more rapid decay of the residual voltage U_{rs} in pre-illuminated films relative to dark-rested film (Fig. 24b)) indicates a slight decrease in the depth of those states. A comparison of room-temperature recovery in TOF and xerographic measurements demonstrates that relaxation of deep centers in pre-illuminated (exposed) films occurs on the same time scale. In other words, the deep gap centers which control the xerographic dark decay and residual voltage are, like the trapping centers discussed in TOF experiments, characteristically metastable.

Band-gap light can, in principle, have two distinct effects on the electronic structure of the mobility gap. Band-gap light can either introduce (generate) new localized states or initiate conversion of traps of small cross section to traps of larger cross section [46]. Consequently, the latter become accessible in deep level spectroscopy only after irradiation. In that sense we may also consider such converted localized states as "new" localized states (created by irradiation).

References

[1] R. A.Street, Appl. Phys. Lett. **41**, 1060 (1982)
[2] R. A. Street, J. Zesch, M. I. Thompson, Appl. Phys. Lett. **43**, 1425 (1983)
[3] R. A. Street, J. Zesch, M. I. Thompson, Appl. Phys. Lett. **43**, 672 (1983).
[4] R. A. Street, C. C. Tsai, M. Stutzman, J. Kakalios, Philos. Mag. B **56**, 389 (1987).
[5] W. E.Spear, W. E.Steemers, H.Mannsperger, Philos. Mag. B **48**, L49 (1983).
[6] E.I. Adirovich , Sov. Solid State Phys. **3**, 2048 (1961) (in Russian).
[7] P. Braunlich, P. Kelly, J.P. Fillard, Thermally Stimulated Relaxation in Solids (Top. Appl. Phys. 37), Ed. P. Braunlich, Springer, Berlin, 1979.
[8] Yu. Gorokhovatsky, G. Bordovskij, Thermally Activational Current Spectroscopy of High-Resistance Semiconductors and Dielectrics , Nauka , Moscow, 1991 (in Russian).
[9] R. A. Street , A. D. Yoffe , Thin Solid Films **11**, 161 (1972).
[10] B.T. Kolomiets , V.M. Lyubin , V.L. Averjanov , Mater. Res. Bull. **5**, 655 (1970).
[11] T. Botila, H.K. Henish , Phys. Status Solidi (a) **36**, 331 (1976).
[12] S.C. Agarwal , Phys. Rev. B **10**, 4340 (1974).
[13] S.C. Agarwal , H. Fritzsche , Phys. Rev. B **10**, 4351 (1974).
[14] P. Muller , Phys. Status Solidi (a) **67**, 11 (1981).
[15] A. A. Kikineshi , V.I. Mikla , I.P. Mikhalko , Sov. Phys. Semicond. **11**, 1010 (1977).
[16] V. I. Mikla , I.P. Mikhalko , Yu. Nagy , J. Phys. Condens. Matter **6**, 8269 (1994).
[17] R. M. Schaffert. Electrophotography. Society of Photographic Scientists and Engineers. (Focal Press, London), 1975, Chapters 1 and 2.
[18] S. O. Kasap, in: Handbook of Imaging Materials, Ed. A.S.Diamond, Marcel Dekker, Inc., New York/Hong Kong, 1991, p. 329
[19] S. M.Vaezi-Nejad, C.Juhasz, Int. J. Electronics **67**, 437 (1989)
[20] S. M. Vaezi-Nejad, Int. J. Electronics **62**, 361 (1987)
[21] M. Abkowitz, R. C. Enck, Phys.Rev B **25**, 2567 (1982)
[22] M. Abkowitz, R. C. Enck, Phys.Rev B **27**, 7402 (1983)
[23] K. K. Kanazawa, I. P. Batra, J. Appl. Phys. **43**, 1845 (1972)
[24] S. W. Ing, Jr., J.H.Neyhart, J.Appl.Phys. **43**, 2670 (1972)
[25] M. Abkowitz, S. Maitra, J. Appl. Phys. **61**, 1038 (1987)
[26] A.R.Melnyk, J. Non-Cryst. Solids **35-36**, 837 (1980)
[27] M. Abkowitz, G. M. T. Foley, J. M. Markovics, A. C. Palumbo, Appl. Phys.Lett. **46**, 393 (1985)
[28] M. Baxendale, C.Juhasz, SPIE Proc. 1253 (1990)
[29] S. O. Kasap, M. Baxendale, C. Juhasz, IEEE Trans. Indust. Appl. **27**, 620 (1991)
[30] S. O. Kasap, J.Electrostat. **22**, 69 (1989)
[31] M. Abkowitz, F. Jansen, A. R. Melnyk, Phil. Mag. B **51**, 405 (1985)
[32] M. Abkowitz, J. Non-Cryst. Solids **66**, 315 (1984).
[33] M. Abkowitz, J. M. Markovics, Solid State Commun. **44**, 1431 (1982)
[34] V. I. Mikla, I. P. Mikhalko, Yu. Yu. Nagy, A. V. Mateleshko, J. Mater. Sci. **35**, 4907 (2001)
[35] V. I. Mikla et al., Materials Science & Engineering B**64**, 1 (1999)
[36] H. Scher, E. W. Montroll, Phys.Rev B **12**, 2455 (1974)
[37] M. Abkowitz, Polym. Eng. Sci. **24**, 1140 (1984)
[38] M. Abkowitz, J. Non-Cryst. Solids **97-98**, 1163 (1987).
[39] M. Abkowitz. Physics of Disordered Materials (Ed. D.Adler, H.Fritzsche, S.R.Ovshinsky), Plenum Press, 1984, p. 483
[40] A. Onozuka, O.Oda, I.Tsuboya, Thin Solid Films **149**, 9 (1987)
[41] S. O. Kasap, J. Phys. D **25**, 83 (1992).
[42] P. J. Warter, Appl. Optic. Suppl. **3**, 65 (1969).
[43] V. I. Mikla, D. G. Semak, A. V. Mateleshko, A. A. Baganich, physica status solidi (a) **117**, 241 (1990).

[44] V. I. Mikla, D. G. Semak, A. V. Mateleshko, A. R. Levkulich, Physics and Technics of Semiconductors **23**, 131 (1989) (in Russian).
[45] S. O. Kasap, in "Handbook of Imaging Materials" edited by A.S.Diamond and D.S.Weiss (Marcel Dekker, Inc., New York, Second Addition, New York, 2002).
[46] B. Polischuk, S. O. Kasap, Viswanath Aiyah, A. Baillie, M. A. Abkowitz, Can. J. Phys. **69**, 361 (1991).
[47] O. Imagava, M. Iwanishi, S. Yokoyama, J. Appl. Phys. **60**, 3176 (1986).
[48] Keiji Tanaka, Current Opinion in Solid State & Materials Science **1**, 567 (1996).
[49] V. M. Lyubin, in: Physics of Disordered Materials (ed. D.Adler, M.Kastner, H.Fritzsche), (New York, Plenum, 1985) p.673.
[50] Keiji Tanaka, phys. status silidi B **246**, 1744 (2009).
[51] Alexander V. Kolobov. Photo-induced Metastability in Amorphous Semiconductors (Willey-VCH, 2003).
[52] Victor I. Mikla, Victor V. Mikla. Metastable States in Amorphous Chalcogenide Semiconductors (Springer, Heidelberg), 2009.
[53] K. Tanaka, "Chalcogenide Glasses", in: Encyclopedia of Materials: Science and Technology. Elsevier Science Ltd (2001), pp. 1123-1131.
[54] Victor I. Mikla, Victor V. Mikla. Trap Level Spectroscopy in Amorphous Chalcogenide Semiconductors (Elsevier Insights, New York, 2010)
[55] V. I. Mikla, J. Phys.: Condens. Matter **8**, 429 (1996).
[56] V. I. Mikla et al., 14th General Conf. GCMD-14, Madrid, 1994, p.1055.
[57] V. I. Mikla et al., 15th General Conf. of the Condensed Matter Devision, Baveno-Stresa, Lago Maggiore, Italy, **20**, p.103 (1996).
[58] V. I. Mikla, Int. Workshop on Advan. Technol. of Multicomponent Solid Films, Uzhgorod, 1996, Book of Abstracts, p.84.
[59] V. I. Mikla et al., Patent USSR 4088420, 1986.
[60] V. I. Mikla et al., Patent USSR 4273793, 1987.
[61] V. I. Mikla et al., Patent USSR 4638891, 1988.
[62] V. I. Mikla, I. P. Mikhalko, Yu. Yu. Nagy, J. Non-Cryst. Solids **142**, 1358 (2001).

*Corresponding author: victormkl836@gmail.com